Earth and Planetary Science Letters 473 (2017) 154–163

Contents lists available at ScienceDirect

Earth and Planetary Science Letters

www.elsevier.com/locate/epsl

The South Atlantic Anomaly throughout the solar cycle

João Domingos [a,b,c,*], Dominique Jault [a], Maria Alexandra Pais [b,c], Mioara Mandea [d]

[a] University Grenoble-Alpes, CNRS, ISTerre, F-38000 Grenoble, France
[b] Physics Department, University of Coimbra, 3004-516 Coimbra, Portugal
[c] CITEUC, Geophysical and Astronomical Observatory, University of Coimbra, Portugal
[d] CNES – Centre National d'Etudes Spatiales, Paris, France

ARTICLE INFO

Article history:
Received 7 November 2016
Received in revised form 24 May 2017
Accepted 3 June 2017
Available online 21 June 2017
Editor: C. Sotin

Keywords:
South Atlantic Anomaly
space weather
PCA
particle flux
L-shell reference frame

ABSTRACT

The Sun–Earth's interaction is characterized by a highly dynamic electromagnetic environment, in which the magnetic field produced in the Earth's core plays an important role. One of the striking characteristics of the present geomagnetic field is denoted the South Atlantic Anomaly (SAA) where the total field intensity is unusually low and the flux of charged particles, trapped in the inner Van Allen radiation belts, is maximum. Here, we use, on one hand, a recent geomagnetic field model, CHAOS-6, and on the other hand, data provided by different platforms (satellites orbiting the Earth – POES NOAA for 1998–2014 and CALIPSO for 2006–2014). Evolution of the SAA particle flux can be seen as the result of two main effects, the secular variation of the Earth's core magnetic field and the modulation of the density of the inner radiation belts during the solar cycle, as a function of the L value that characterises the drift shell, where charged particles are trapped. To study the evolution of the particle flux anomaly, we rely on a Principal Component Analysis (PCA) of either POES particle flux or CALIOP dark noise. Analysed data are distributed on a geographical grid at satellite altitude, based on a L-shell reference frame constructed from the moving eccentric dipole. Changes in the main magnetic field are responsible for the observed westward drift. Three PCA modes account for the time evolution related to solar effects. Both the first and second modes have a good correlation with the thermospheric density, which varies in response to the solar cycle. The first mode represents the total intensity variation of the particle flux in the SAA, and the second the movement of the anomaly between different L-shells. The proposed analysis allows us to well recover the westward drift rate, as well as the latitudinal and longitudinal solar cycle oscillations, although the analysed data do not cover a complete (Hale) magnetic solar cycle (around 22 yr). Moreover, the developments made here would enable us to forecast the impact of the South Atlantic Anomaly on space weather. A model of the evolution of the eccentric dipole field (magnitude, offset and tilt) would suffice, together with a model for the solar cycle evolution.

1. Introduction: the particle flux in the South Atlantic Anomaly

Electromagnetic radiation and charged particles from the Sun constantly reach the Earth. The Sun–Earth interplanetary space is populated with magnetic fields and particles carried by the solar wind to form a highly dynamic electromagnetic environment around the Earth. This environment interacts with the Earth's magnetic field, and this interaction is of a high complexity due to the underlying physical processes and the diversity of the temporal and spatial scales that characterize geomagnetic field sources.

One important ingredient in analyzing the Sun–Earth electromagnetic interaction is the morphology and temporal variations of the main geomagnetic field, originating from magnetohydrodynamic processes in the Earth's outer core. This contribution to the measured magnetic field is complemented by the lithospheric field (however, not of interest in our study, as considered as constant over the temporal scales we are interested in), and the external fields, linked to processes in the ionosphere and magnetosphere. The observation and analysis of the main characteristics of the geomagnetic field at the Earth's surface, together with their variations, have enabled the elaboration of data-based models and numerical geodynamo simulations that have been successful in providing explanations for features of the field such as its predominantly dipolar character, secular variation and field reversals (e.g. Christensen et al., 2010; Olson et al., 2014). One of the striking characteristics of the present geomagnetic field is a region denoted the South Atlantic Anomaly (SAA), where the total field intensity is unusually low. There, the field intensity reaches less than 60% of the field strength at comparable latitudes. The loca-

* Corresponding author.
E-mail address: rosadomj@univ-grenoble-alpes.fr (J. Domingos).

http://dx.doi.org/10.1016/j.epsl.2017.06.004
0012-821X/

tion of the minimum has moved from Southern Africa to South America over the last 300 yr (Mandea et al., 2007; Hartmann and Pacca, 2009). The total dipole strength has diminished by 9% from 1840 to 2015, although the field decrease occurs non-uniformly over the globe. Presently, the decrease of the field intensity, which is accurately mapped from low Earth orbiting satellites, is also observed in the Southern African–Southern Atlantic region (Finlay et al., 2016). The weakness of the field intensity in the SAA is caused by a patch of opposite magnetic flux compared to the dipole direction at the core–mantle boundary (Bloxham et al., 1989; Olson and Amit, 2006), stressing that the main contribution to the SAA is internal. This inverse flux patch at the core–mantle boundary (CMB) has been growing continuously from the beginning of the 19th century (Jackson et al., 2000).

We can try to dispense with some of the complexity of the main field to describe the Earth's magnetosphere. The large-scale geomagnetic field is conveniently approximated as a dipole offset from the Earth's centre (e.g. Fraser-Smith, 1987), a simplified model which already takes into account most of the SAA (e.g. Heynderickx, 1996). In this dipole reference frame, the drift shells that trap charged particles are described by the equation $r = L \sin^2 \theta$, where θ is the colatitude, r is distance from the dipole centre and Earth's radius is unit of length. Each value of the L parameter defines a separate shell. The particles population of the shells is depleted through interactions in the atmosphere and the flux of energetic protons (in the range $\sim$ 10 MeV–1 GeV) is particularly high for L values between around 1 and 3 (with maximum at about $L = 1.5$), in the so-called inner radiation belt (Selesnick et al., 2014). Due to the dipole offset towards the western Pacific, the inner Van Allen radiation belt gets closer to the Earth over the SAA region. This means that the mirror points where trapped particles bounce in their spiralling around field lines lie at much lower altitudes there than elsewhere (Vernov et al., 1967; Gledhill, 1976).

The eccentric dipole is currently offset from the Earth's centre by about 550 km in a direction approximately 22°N, 140°E. This distance is steadily increasing and the location of the eccentric dipole centre is drifting in the westward direction and slightly northward. In the antipodal direction, which corresponds to the location of the SAA, the drift shells get closer to the Earth's surface and move mainly westward and slightly southward. We thus have three ways to describe the SAA position, either as the location of a local minimum of the magnetic field intensity (for a given altitude), as the place where the flux of charged particles is maximum, or as the location of the antipodal point of the geographic location of the eccentric dipole (Heynderickx, 1996). These three descriptions are obviously connected, as the high particle counts observed in the SAA region are correlated with the local weakness of the Earth's magnetic field which can be explained in terms of the departure of the eccentric dipole. Despite this fact, the three approaches to define the SAA provide images which are not completely identical, the shape and even evolution of the anomaly being different. This provides the motivation for a dedicated study of the SAA morphology and evolution.

So far we have outlined the contribution of the main geomagnetic field morphology for the intense radiation fluxes met by satellites over the South-Atlantic Brazilian coast region. An accumulation of satellite data since the 60s has brought to light decadal and sub-decadal variability of the SAA, seemingly due to particle feeding and depletion mechanisms in the inner radiation belt (e.g. Gledhill, 1976; Selesnick et al., 2014). The neutral atmosphere expands during the ascending phase of the solar cycle and, at altitudes above 100 km, its density increases (Solomon et al., 2013). As a result, in regions where mirror points are low enough, protons are removed from the inner belt through nuclear collisions with atmospheric neutral particles (Gledhill, 1976), explaining why the particle flux in the SAA region is anti-correlated with the solar activity as measured by the 10.7 cm radio flux of the Sun (Fürst et al., 2009; Casadio and Arino, 2011; Qin et al., 2014). This effect is maximized for the low values of L that correspond to the highest energy proton shells (Vacaresse et al., 1999). Different source mechanisms are thought to be responsible for feeding the inner-belt with lower ($\lesssim$ 40 MeV) and higher energy protons, the trapping of solar protons for the former and the beta decay of neutrons created as a result of the interaction of galactic cosmic rays with the upper atmosphere (CRAND mechanism) for the latter (Selesnick et al., 2014). Finally, an annual variation of the SAA has recently been described (Schaefer et al., 2016).

Also important to stress is the hazard due to the unusually high flux of high energy particles in the SAA region, resulting in significant space weather effects in space, such as satellite outages (Heirtzler, 2002) or even on ground, as in communications, induced currents in pipelines and transmission lines (Pulkkinen et al., 2012; Boteler and Pirjola, 2014). High energy protons affect the oscillator of space clocks in the SAA region (Belli et al., 2015; Capdeville et al., 2016). They also hit the detectors of stellar cameras on board Low Earth Orbiting (LEO) satellites, such as CoRoT (Auvergne et al., 2009). All these practical concerns together with a large amount of available data, make studies contributing to a more accurate description of the SAA both relevant and timely.

Here, we are interested in using data sets provided by different platforms. We take advantage of information provided by different satellites orbiting the Earth and carrying diverse instruments. For the particle flux studies we have used two different data sets, the proton omni-directional detections from the POES NOAA 15 satellite (Evans et al., 2008) and the dark noise data from the CALIPSO satellite (Noel et al., 2014). In order to describe the main magnetic field and the evolution of the eccentric dipole, the most recent CHAOS model, CHAOS-6, was used (Finlay et al., 2016). Unlike most previous authors who chose either Gaussian (e.g. Konradi et al., 1994) or Weibull (Fürst et al., 2009) functions to describe the shape of the SAA, we do not assume a priori geometry of the anomaly. Spatial patterns emerge instead from the Principal Component Analysis (PCA) of either POES particle flux or CALIOP dark noise data, which are distributed on a geographical grid.

The paper is organized as follows. The data and models are described in the next section. Thereafter, in section 3, we present our methods to investigate the data sets. Results are presented in section 4. Finally, we discuss these results and conclude.

2. Data and models available

2.1. CHAOS-6 model

The CHAOS-6 model (Finlay et al., 2016) is the latest in the CHAOS series of Earth magnetic field models (Olsen et al., 2006). It combines data from some 160 ground observatories (annual differences of revised monthly means) together with satellite data, including the most recent Swarm data, collected from a 3-satellite constellation in orbit since end of 2013 (Olsen et al., 2015). The time variation of the field is described by cubic B-splines with 6 months knot spacing, from 1996 to 2016.5. The actual temporal resolution is not so high because of regularisation. The model is precise enough to resolve peaks of secular acceleration (second time derivative of the field) separated by about 3 yr, up to harmonic degree $n = 15$. We have used it to identify trends of the SAA that depend on the morphology of the main field, such as the latitude and longitude of the location of minimum field intensity and the time evolution of this minimum. The evolution of the minimum depends on the spherical surface on which it is calculated. At the surface of the Earth, a westward drift of 0.30°/yr

together with a slight northward drift of 0.008°/yr and an intensity decrease of 20.98 nT/yr can be identified. The same calculations at 800 km, give a westward drift of 0.17°/yr, a now southward drift of 0.020°/yr and an intensity decrease of 8.90 nT/yr. To complement this analysis, we can also look at the movement of the antipodal location from the eccentric dipole approximation, which gives a westward drift of 0.30°/yr and a southward drift of 0.056°/yr. The eccentric dipole part of the field depends on spherical harmonic coefficients up to degree $n = 2$ as in Fraser-Smith (1987). Note that there are other definitions, as expounded by Lowes (1994). In this study we used the coefficients provided by the CHAOS-6 model to obtain the latitude–longitude coordinates in the reference frame of the dipole and to calculate the Mcllwain L-shells (Mcllwain, 1961). The slow time evolution of the L-shells, or L-lines, plotted on a surface, reflects the movement of the eccentric dipole. As such, they can be considered as a reference frame which moves along with the field. In section 3.2, the L-shells together with the magnetic field intensity from CHAOS-6 are used to define the grid on which the principal component analysis is applied.

2.2. POES – particle flux data

The particle flux data used in this paper are those provided by the POES (Polar Orbiting Environmental Satellites) NOAA-15. The satellite orbits at a $\sim$ 820 km slowly decreasing altitude and is equipped with the SEM-2 (Space Environment Monitor) detectors. In this study we have used the SEM-2 omni-directional detectors, which provide four different energy ranges ($>$ 16, $>$ 36, $>$ 70 and $>$ 140 MeV). The results below concern $>$16 MeV detections. The SEM-2 has other detectors which measure less energetic protons, but in narrow energy ranges. Here, we are most interested by the flux of high energy protons, which populate the inner radiation belts. We have analysed 16.5 yr of data, from the 1st of June of 1998 until the end of 2014, including the maximum of solar cycle 23 (2000–2002) and the minimum of solar activity between cycles 23 and 24 ($\sim$ 2009). We use monthly data charts with a spatial grid spacing of 2.5° in both latitude and longitude.

Qin et al. (2014) have recently analysed the proton flux measured by NOAA-15 from 1999 to 2009. They used a Gaussian function to approximate the geometry of the SAA and investigated the variability of the anomaly on decadal time-scales. They found that the westward drift of the SAA is more rapid during the solar minimum than during the solar maximum. Back and forth movement of the SAA during the solar cycle occurs both in longitude and in latitude. Enhanced westward drift is accompanied by northward displacement of the SAA.

Zou et al. (2015) also relied on NOAA POES protons observations to investigate the short-term variations of the inner radiation belt in the South Atlantic region. Using Gaussian functions to describe the SAA geometry, they found that the proton flux in the SAA decreases a few per cent after large geomagnetic storms. They also drew attention to a 120-day oscillation in the proton flux that is simply caused by variations in the altitude of NOAA-15.

2.3. CALIOP – dark noise data

As a supplementary data set to the particle flux provided by the POES mission, the CALIOP (Cloud-Aerosol Lidar with Orthogonal Polarization) instrument readings, on board of the CALIPSO (Cloud-Aerosol Lidar and Infrared Pathfinder Satellite Observation) mission were used. The data provided by the CALIOP instrument are not strictly particle flux, they are what is called dark noise. In photomultipliers and avalanche photodiodes used in detectors, there is always some background signal even in the absence of incident photons, caused by random generation of electrons in the system, which is called 'dark noise' and is handled in a statistical framework. The CALIOP detectors show a significant increase of dark noise in the region of SAA (Hunt et al., 2009). This interference is caused by the particle flux increase in the region, so it can be used as a substitute. The CALIPSO satellite orbits at approximately 705 km altitude, about 100 km lower than the POES satellite. For this particular data series we only had 8 yr of available measurements, from 2006 to 2014. In the same manner as for the POES data, we analysed monthly data charts with a grid spacing of 2.5°. This shorter time series makes it complicated to extract relevant patterns and time functions from the data, particularly if related with the solar cycle.

Noel et al. (2014) have previously reported the solar cycle influence on CALIOP dark noise for the same time period. They estimated for the westward drift a speed of 0.3°/yr, which is in agreement with previous studies about the particle flux and the time evolution of the main field. A variation of the area of the anomaly was also observed, which consists in a cyclic evolution in sync with the solar cycle.

3. Methods

3.1. Principal Component Analysis applied to SAA

A number of studies have tested specific models for the SAA spatial distribution, by fitting the data with *a priori* analytical functions. Gaussian functions were proposed to describe the spatial distribution of particle flux over the South Atlantic region, both longitudinally and latitudinally (e.g. Casadio and Arino, 2011; Qin et al., 2014). To account for an apparent West–East morphological asymmetry, Weibull and Gumbel functions have also been tested (Fürst et al., 2009; Hell, 2010). Here, we follow a different approach by making use of a statistical non-parametric method, i.e., that does not assume any particular spatial or temporal dependences for the data. It is nonetheless implied that the spatial and temporal variations of the SAA can be separated. The method, known as Principal Component Analysis (PCA), provides a description of data in terms of a small number of spatial patterns (the Empirical Orthogonal Functions, EOFs) and corresponding time series (Principal Components, PCs), which together account for as much of the observed variability as required. The analysis is based on a spectral decomposition of the data correlation matrix and the individual modes (pairs of spatial structures and corresponding temporal series) are by construction decorrelated in space. The main references for PCA applications similar to ours, can be found in the fields of meteorology and oceanography, where the method was largely used to isolate and characterize features such as the North Atlantic Oscillation (NAO), the El Niño–Southern Oscillation (ENSO) or the Pacific–North America teleconnection pattern (PNA) (e.g. Preisendorfer, 1988; Von Storch and Navarra, 1995). In the field of geomagnetism, we can find a closely related, recent, application in Pais et al. (2015), in search for decorrelated modes of the quasi-geostrophic liquid core flow.

Let $\mathbf{X}$ be the data matrix with snapshots of gridded data values of either POES particle flux or CALIOP dark noise:

$$\mathbf{X} = \begin{bmatrix} X_{1,1} & X_{1,2} & \cdots & X_{1,n} \\ X_{2,1} & X_{2,2} & \cdots & X_{2,n} \\ \vdots & \vdots & \ddots & \vdots \\ X_{m,1} & X_{m,2} & \cdots & X_{m,n} \end{bmatrix} \tag{1}$$

where $X_{i,j}$ is the data value attributed to grid point j at epoch i. Index j takes values from 1 to the total number n of grid points, and index i takes values from 1 to the total number m of epochs considered in the analysis. The PCA identifies features of the spatial

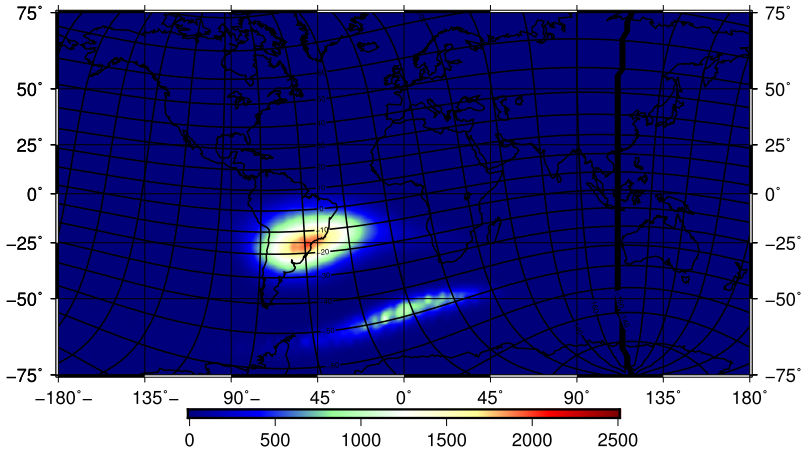

Fig. 1. POES particle flux data for December 2014 with eccentric dipole grid representation overlaid.

distribution of particle flux or dark noise data that evolve correlated in time. Such spatial structures (EOFs) are the eigenvectors of the covariance matrix $\mathbf{C}_X = \mathbf{X}^T\mathbf{X}$, real and symmetric. We denote $\mathbf{P}$ the matrix that has the eigenvectors of $\mathbf{C}_X$ as columns, ordered according to the amplitude of (real, positive) eigenvalues of $\mathbf{C}_X$, and $\mathbf{U}$ the matrix with eigenvectors of $\mathbf{X}\mathbf{X}^T$ as columns. Both $\mathbf{P}$ and $\mathbf{U}$ are orthogonal matrices that factorize $\mathbf{X}$ according to:

$$\mathbf{X} = \mathbf{U}\mathbf{\Lambda}\mathbf{P}^T, \tag{2}$$

known as Singular Value Decomposition of $\mathbf{X}$. Matrix $\mathbf{\Lambda}$ is a $m \times n$ rectangular diagonal matrix, with all entries $\Lambda_{i,j}$ with $i \neq j$ being zero and all entries $\Lambda_{i,i}$ equal to the square roots of the eigenvalues of $\mathbf{C}_X$ (or singular values of $\mathbf{X}$), ordered from the highest to the lowest. Matrix $\mathbf{A} = \mathbf{X}\mathbf{P} = \mathbf{U}\mathbf{\Lambda}$ is the matrix of amplitudes. Denoting A^k the kth column of $\mathbf{A}$ and P^k the kth row of $\mathbf{P}^T$ (or transpose of kth column of $\mathbf{P}$), then the data matrix can be decomposed into n PCA modes according to:

$$\mathbf{X} = \sum_{k=1}^{n} A^k \otimes P^k \tag{3}$$

where the symbol '$\otimes$' denotes the dyadic product between column vector A^k and row vector P^k. A^k is the kth-order PC: the vector with amplitudes of PCA mode-k for the whole time interval analysed, with high (positive or negative) coefficient values at epochs when mode-k has a strong inprint. P^k is the kth-order EOF: the spatial pattern localising the geographic regions that take part in mode-k.

The PCA modes are also named 'variability' modes, because of the role of P^k eigenvectors in the spectral decomposition of the variance–covariance matrix $\mathbf{C}_X$. The percentage of variability (or variance) accounted for by mode-k in this decomposition is (e.g. Hannachi et al., 2007)

$$f_k = \frac{100\,\Lambda_{k,k}^2}{\sum_{i=1}^{n} \Lambda_{i,i}^2}. \tag{4}$$

Note that mode-k contributes to $\mathbf{C}_X$ spectral decomposition with weight $\Lambda_{k,k}^2$ and to the PCA decomposition of $\mathbf{X}$ with weight $\Lambda_{k,k}$.

3.2. Reference frames

As mentioned before, one way to analyse and track the evolution of the SAA is to monitor the location and orientation of the eccentric dipole. This is done by selecting the spherical harmonics up to degree 2 of a given magnetic field model, namely CHAOS-6 in this study. Departure of the eccentric dipole from an axial dipole suffices to explain the main part of the SAA, although there are some slight differences in its shape. In fact, a westward drift of the anomaly of about 0.3°/yr is retrieved from the movement of the eccentric dipole, which is consistent with estimates obtained directly from particle flux data (e.g. Fürst et al., 2009; Noel et al., 2014; Schaefer et al., 2016). It is enlightening to describe the anomaly in this way, the interaction of charged particles with the main field can be considered in a dipole field geometry (though tilted and displaced from the Earth's centre). In this study we took advantage of this feature to construct a reference frame that gets rid of effects due to changes of the tilt and/or the centre of the main field dipole and concentrates on effects that can be explained using the well-known dynamics of charged particles trapped in a dipolar magnetic field (Vernov et al., 1967; Gledhill, 1976).

3.2.1. Eccentric dipole reference frame

Some tests have been carried out in the search for an adequate reference frame, one that on the one hand can minimise the appearance of undesired data, and on the other hand can properly characterize the main spatial and temporal features of the SAA using the PCA method. Using a regular geographic latitude–longitude grid we found that a patch of particle flux can be detected at times of high solar activity in a region South of the anomaly (see Fig. 1).

To remove this patch of the particle flux, not relevant for this study, and not crop any portion of the SAA patch, a new latitude–longitude grid with the orientation based on the inclination and displacement of the eccentric dipole was used, the 'dipole reference frame'. Contours of this grid can be seen in Fig. 1, overlaid on top of a snapshot of the POES particle flux data, to compare with the regular geographic latitude–longitude grid (vertical and horizontal lines). In this particular snapshot of POES particle flux for December 2014, we can see the undesirable particle flux region to the South of the anomaly, and the way the dipole reference frame allows to crop around it. To account for the displacement of the eccentric dipole, this reference frame was recalculated for each instance of the particle flux data, using the CHAOS-6 model. In this way, the frame follows the movement of the anomaly, at least that component due to the secular change of the main field.

3.2.2. L-shell reference frame

Here we use the *a priori* knowledge that trapped particles drifting in a certain L-shell have their lowest altitude mirror points where the magnetic field intensity is also minimum (Gledhill, 1976). This suggests that the most physically meaningful coordi-

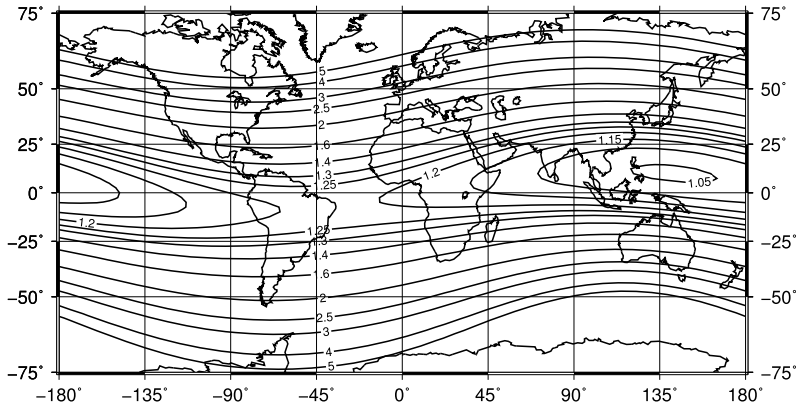

Fig. 2. L-shells at 800 km altitude; computation is based on the CHAOS-6 model.

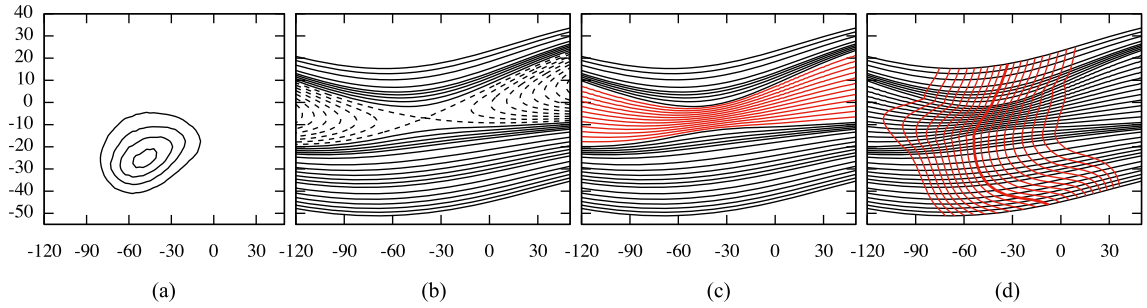

Fig. 3. Contours of the particle flux anomaly (a). Representation of the L-shell reference frame construction process: removal of $L < 1.22$ contours as shown by dashed lines (b); new lines defined by interpolating lines in red (c); vertical axis created from thick red line of $|B|_{min}$ together with other $|B|$ contour lines (d). (For interpretation of the references to colour in this figure legend, the reader is referred to the web version of this article.)

nates to map the particle flux data are L and the field intensity $|\mathbf{B}|$. In a dipole field, L values can be calculated as,

$$L = \frac{r}{\cos^2 \lambda}, \tag{5}$$

where r is the distance in Earth radii to each point in the field line and λ is the geomagnetic latitude, computed based on the eccentric dipole approximation (dipole and quadrupole spherical harmonic coefficients). As in section 3.2.1, the grid values (in this case L and $|B|$) were recalculated for each instance of the particle flux data. This representation identifies each particular magnetic field line by the distance in Earth radii when it crosses the magnetic equator. When considering all field lines with the same L value, we construct L-shells. These shells of toroidal shape circle the Earth and are organized about the axis of the eccentric dipole. Due to the dipole displacement with respect to the Earth's centre, there are L-shells that intersect constant altitude surfaces in some angles of longitude only (see in Fig. 2, the shells that cut the 800 km altitude surface between 80° W and 0°). This behaviour can be seen in Fig. 2, where some lines do not cover all longitude values, representing an area where the L-shell is located beneath the considered altitude.

The L-shells description is appropriate to discuss the particle flux in the upper atmosphere. Trapped charged particles, such as protons and electrons move along L-shells, bouncing between mirror points North and South of the magnetic equator, and drifting around the Earth. It is a useful simplification to consider separately the particle flux of the different L-shells. The particle flux distribution is related to the Sun's activity, and varies according to the solar cycle (Vacaresse et al., 1999). Because the trapped particle motions are well described in terms of L-shells, it seems logical to study the evolution of the particle flux using the L-shell representation.

In order to properly describe the particle flux, we need another parameter besides the L value. Although a charged particle population can be associated to each L-shell, the mirror points for the particles motion depend on longitude. As we discussed before, the magnetic field intensity affects the penetration of energetic particles, and so, for each L line at a certain altitude, a higher particle flux is expected where the magnetic field has its minimum. With this in mind, we have drawn the location of the minimum magnetic field intensity as a function of L and from this contour we have been able to define a new coordinate.

In Fig. 3 we can see a step by step representation of the reference frame construction. In order to properly map the region of interest, certain L-shells had to be removed, namely the ones that did not properly cover the entire longitudinal range. At the altitudes concerned by our data we removed all lines with $L < 1.22$ (Fig. 3b). A set of 12 lines were drawn to fill the void left by the removed L contours (Fig. 3c). This was done by interpolating linearly the difference between the two innermost L-shells for each fixed longitude value. For each one of L contours and interpolating lines, which globally define the L coordinate, we located the point of minimum field intensity, as calculated using the CHAOS-6 model up to degree 13. The set of all these points gives the thick red line on Fig. 3d. Finally, a set of lines were drawn, shifted from the minimum $|B|$ contour by a multiple of $B_{step} = \Delta|B|$, in both East and West directions. They define the B coordinate according to:

$$B_i^j = B_{min}^j \pm B_{step}\, i^2 \tag{6}$$

where B_i^j is the value of $|B|$ in L-shell j (L_j) in position i away from the centre line. B_{min}^j is the minimum $|B|$ value for line L_j and B_{step} is a constant to set the spacing of the B grid coordinate.

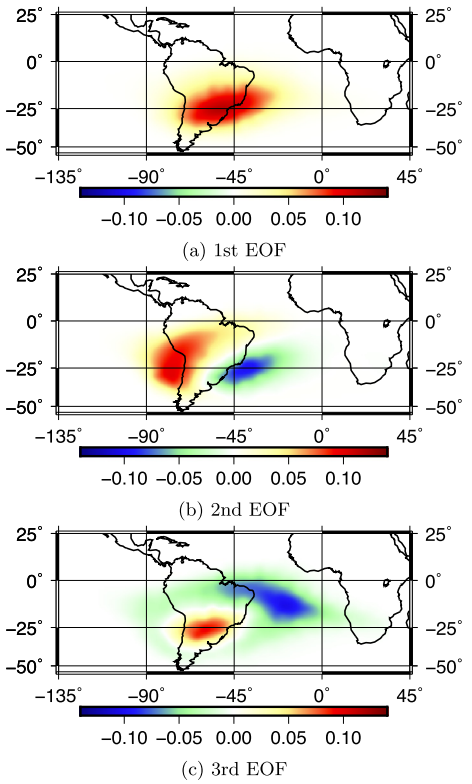

Fig. 4. The first three spatial patterns from the PCA analysis of POES data between 1998 and 2014, using the dipole reference frame and represented in the regular geographic grid. Percentage of variability, f_i, from the first to the last: 99.46, 0.38 and 0.11.

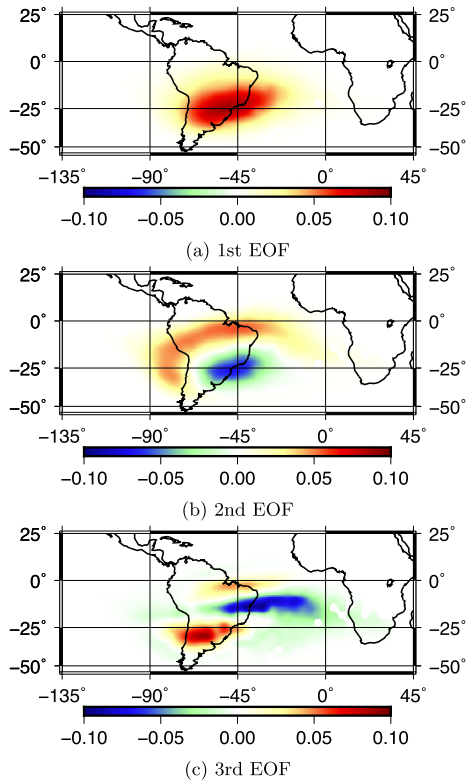

Fig. 5. The first three spatial patterns from the PCA analysis of POES data between 1998 and 2014, using the L-shell reference frame and represented in the regular geographic grid. Percentage of variability, f_i, from the first to the last: 99.64, 0.28 and 0.02.

The increments of B defining the grid have been customised to the variation of B near its minimum (where $\partial B/\partial i = 0$) on each L line.

Both grids define a new coordinate system (the 'L-shell reference frame') for the region where the SAA is located, covering $[-135°{:}45°]$ in longitude and $[-50°{:}25°]$ in latitude. The approximate average grid spacing is 2.5°.

4. Results from the PCA analysis

When applying the PCA method, we can choose to either keep or remove the mean particle flux at each grid point, averaged over the whole time interval. In this study we have chosen to represent and discuss the results with the mean flux distribution retained in the calculation, since this leads to a clearer interpretation of results, enabling a better description of the physical source for each mode.

The particle flux data from the POES satellite, for the period between 1998 and 2014, have been analysed. Fig. 4 shows the spatial structures (or EOFs) of the first three modes obtained through the PCA decomposition of the data using the dipole grid described in section 3.2. Each of the three modes shows interesting spatial and temporal structures, which can be understood in the light of physical mechanisms involving trapped radiation. All together, they explain more than 99.9% of the total data variability (see eq. (4)). The first mode shows a (monopolar) structure of particle flux intensity (Fig. 4a) with the same shape as the mean SAA and an associated time oscillation between a maximum and a minimum of intensity (Fig. 6a).

The second mode, showing a bipolar spatial structure (Fig. 4b), represents a superposition of a steady westward drift and an oscillation of about 11 yr period (Fig. 6a). The range of variation of mode 1 is just about a factor 2 larger than that of mode 2, both modes showing a time oscillation with approximately an 11 yr period. Keeping the time average helps to define the spatial structure of mode 1 (which is also present in the mean) thus allowing for a better separation of the two modes. Finally, a change in the geometry of the anomaly can be represented by the third mode (Fig. 4c). As we show below, this mode can be significantly reduced in terms of its fraction of variability, if the more adequate L-shell reference frame is used.

When analysing the decomposition of the same data, but using the L-shell reference frame (Fig. 5), the first mode (Fig. 5a) is much the same, with an identical time series (Fig. 6b). This has been expected as the change of reference frame does not affect the calculation of the total flux. The second mode, which reflects motions of the anomaly, strongly depends on the reference frame and the grid choice. Both its spatial structure (Fig. 5b) and its evolution are affected. We note in section 4.2 below that calculating this mode on the L-shell reference frame is the appropriate way to understand its origin. The third mode is also very different in the two reference frames. This might have been expected because it accounts for geometrical variations of the anomaly and the transformation between the dipole and the L-shell reference frames introduces distortions. The third mode in the L-shell reference frame has a clear tripolar structure. Most of the variability of the anomaly is represented by the first two modes and the third mode is significantly less energetic when calculated on the L-shell reference frame (0.02% of the variability) than when calculated on the dipole reference frame (0.11% of the variability).

Applying PCA to only that data from POES that is concurrent with the CALIOP data, the modes and time series (see Fig. 7) closely match. This leads us to believe that with a long enough

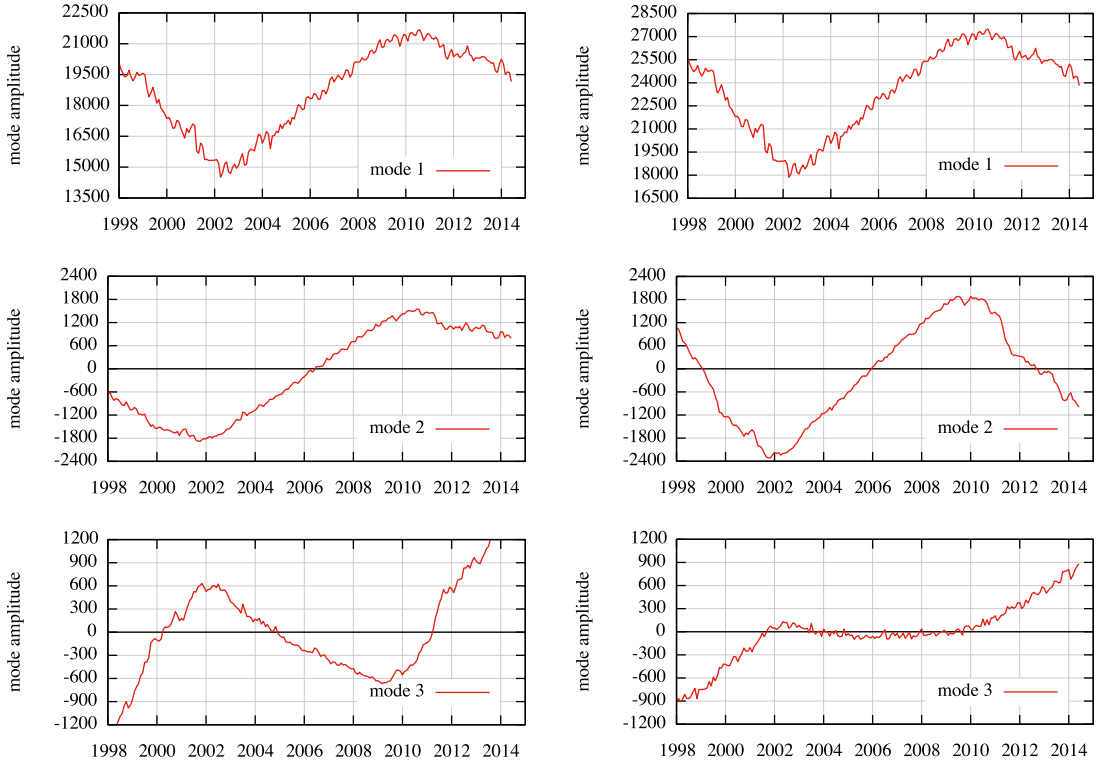

(a) PCs using the dipole reference frame.

(b) PCs using the L-shell reference frame.

Fig. 6. Time series corresponding to modes in Figs. 4 and 5 for the POES particle flux data.

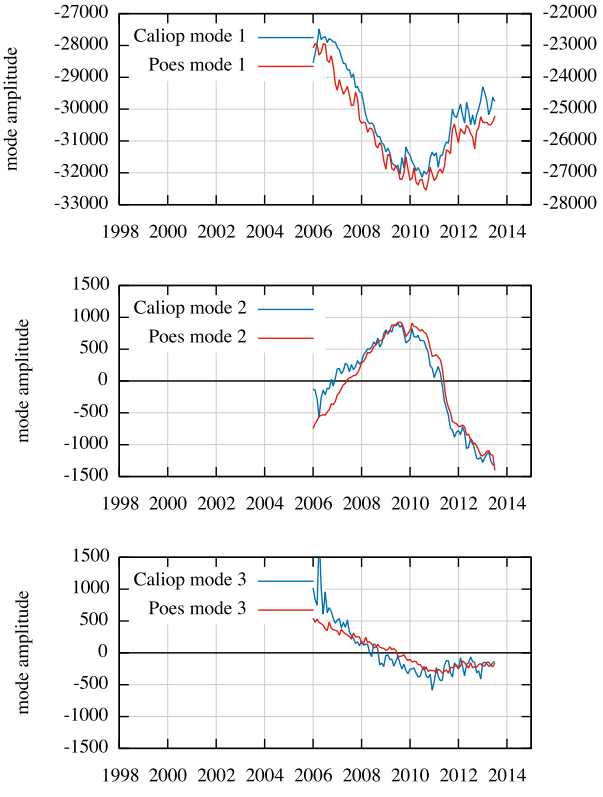

Fig. 7. Modes amplitude for CALIOP dark noise data and POES particle flux data for the same time interval.

time series, the dark noise data could be interpreted in the same way as particle flux data.

4.1. The first mode: modulation of the global flux of trapped protons by the solar cycle

The first mode of either PCA decompositions is related to the global increase and decrease of particle flux in the inner Van Allen belt. On the top of Fig. 6b we can see the time series of the first mode from the PCA decomposition of the POES data. Comparing the time variation of this mode with the thermospheric density evolution (Fig. 8), we can clearly see the response of the flux of particles to the evolution of the thermospheric density. Thermospheric density is directly correlated with the Sun's activity, as a result of heating driven by solar radiation, showing the same time evolution as the solar cycle (Solomon et al., 2013). Density increase at high altitude as the atmosphere expands during solar maxima leads to more frequent collisions between the trapped energetic protons and atmospheric atoms. As a result, the trapped proton stocks are depleted during maxima of the solar cycle. We identified a 17 month lag between the time series of the first mode and the thermospheric density variation.

4.2. The second mode: bipolar oscillation in the location of the maximum protons flux

As seen in the two PCA decompositions from POES particle flux data with the different grid choices, the second mode is also enslaved to the solar cycle. There is a clear oscillation in the time series (Figs. 6a and 6b), following the solar cycle. The internal field is responsible for a westward drift of the anomaly, which can be clearly seen in the time series in Fig. 6a, superimposed with an oscillation. This trend is already slightly removed by using a reference frame that follows the evolution of the eccentric dipole, but in the L-shell reference frame, it is almost completely removed (Fig. 6b). In Fig. 9 we can clearly see the gradual removal of the drift component with the choice of reference frame.

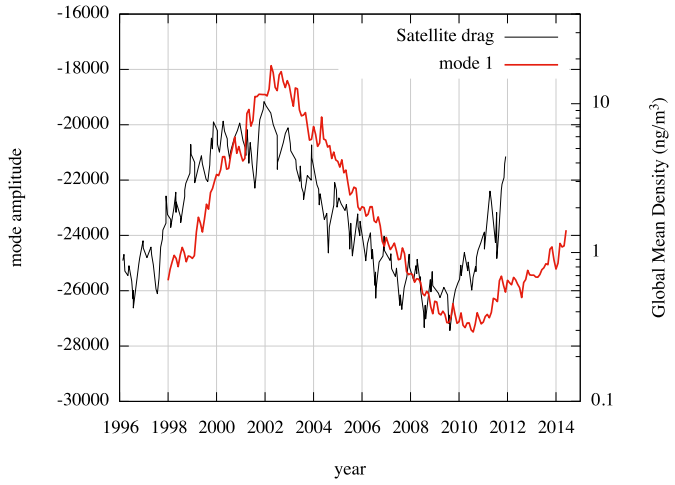

Fig. 8. Time series of the first PCA mode of POES L-shell reference frame and the thermospheric density. Atmospheric data retrieved from Solomon et al. (2013).

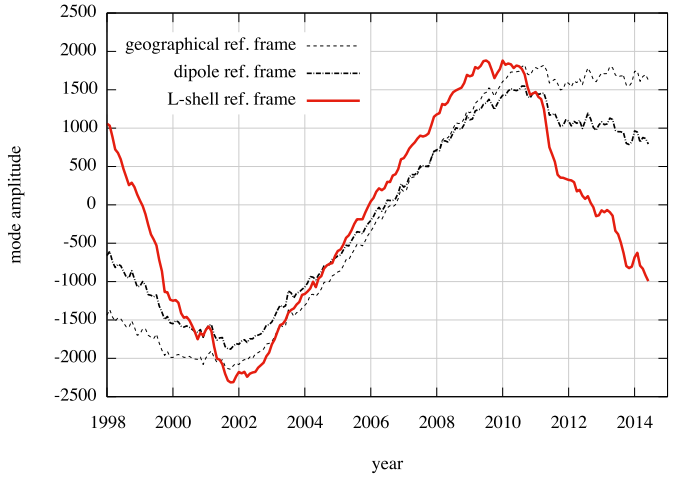

Fig. 9. Time series of the second mode for POES: comparison between a regular geographical grid (thinner dashed line), the dipole reference frame (thicker dashed line) and the L-shell reference frame (bold red line). (For interpretation of the references to colour in this figure legend, the reader is referred to the web version of this article.)

The dipole grid takes into account the westward movement of the eccentric dipole, but it is not able to properly account for the direction in which the particle flux moves. This movement is dictated by the location of the minimum intensity of the magnetic field in each L-shell. The L-shell reference frame takes into account exactly this, and we are able to almost completely separate the westward drift and the North–South oscillation driven by the Sun's activity.

With the internal field westward motion almost entirely removed, the L-shell mode shows a clear North–South behaviour. Along the solar cycle, different L-shells are differently populated by energetic particles. The shells with low L values are the most affected by depletion mechanisms during the solar maximum (Miyoshi et al., 2000). As a result the maximum of the anomaly is displaced towards a higher L value. This variation of L-shell population, together with the variation of the position of the minimum of the magnetic field intensity in these L-shells (Vernov et al., 1967; Gledhill, 1976), leads to the oscillation represented by the second mode. A 10 month phase lag was obtained when the time series was compared with the thermospheric density variation.

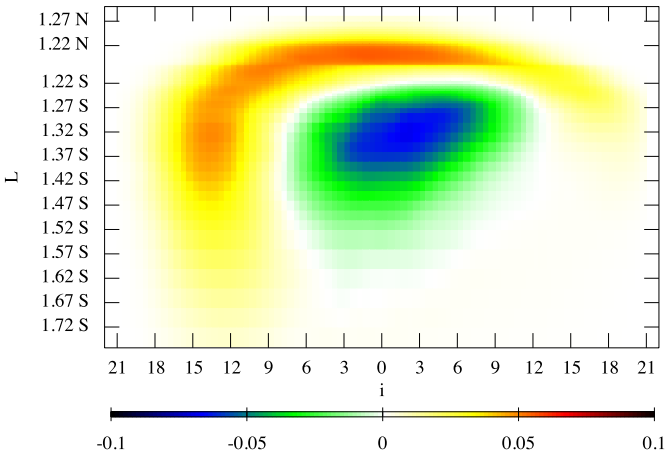

Fig. 10. The spatial patterns from the second mode of the PCA analysis of POES data between 1998 and 2014, using the L-shell reference frame and represented in the L–B_{min} grid. In this representation equation (6) is used, with i values ranging between 0–21 and the B_{step} equals 10.

In Fig. 10 the spatial pattern of the second mode is represented in the L–B_{min} space. Let us note that a sudden change seems to separate the L-shells 1.22 N and 1.22 S. However, this is not a real feature, as in this region the interpolated L-shells have very close values of L whereas in the regular geographical space they have larger spacing. The break in the spatial pattern is the result of squeezing the smooth pattern in that region.

5. Discussion and conclusions

Evolution of the SAA particle flux can be seen as the result of two main effects, the secular variation of the Earth's magnetic field and the modulation of the protons density of the inner Van Allen radiation belt during the solar cycle. The internal geomagnetic field, due to a dynamo inside the Earth's liquid core, is responsible for the observed westward drift. A main point coming out from this study is the identification of a reference frame, which we call L-shell reference frame, depending only on the main field. In this frame, the particle flux data can be decomposed into stationary modes with a physical interpretation in terms of mechanisms of feeding (CRAND, trapping of solar protons, ...) and depletion (nuclear collisions with atoms of the neutral atmosphere) of energetic protons inside the inner radiation belt. This provides for the separation of internal and external effects. We have identified the modes that represent evolutions related to solar effects. Both the first and second modes have a good correlation with the thermospheric density, which varies with the solar cycle. The first mode represents the intensity variation of the global particle flux in the inner Van Allen belt. The second mode represents the movement of the peak of the proton flux between different L-shells. A different phase lag was identified when comparing both time series with thermospheric density evolution. A 17-month delay for the first mode and 10 months for the second. This difference is not necessarily a product of a small time resolution or the method itself. In fact, the particle flux in different L-shells responds to the solar cycle with different time lags (Miyoshi et al., 2000). We have found that the position of the anomaly at solar maximum is 2.6° South and 0.9° East from its position at solar minimum. It corresponds to a change from $L = 1.32$ at solar minimum to $L = 1.35$ at solar maximum.

Once these modes are transformed back into the geographic frame, secular change of the main field combine with variations in the L-shells proton population. The westward drift rate as well as latitudinal and longitudinal solar cycle oscillations are well recovered in agreement with results from other recent studies (e.g.

Qin et al., 2014). In Qin et al. (2014), they identify a 685 days time delay between the F10.7 solar index and the proton flux longitudinal evolution. They obtain these results studying protons with energies > 70 MeV, so no direct comparisons can be made with our results which focus on protons with energy > 16 MeV. By moving the reference frame together with the eccentric dipole, which represents the main part of the geomagnetic field, we account well for the westward motion of the anomaly. Conversely, on a 20 yr time scale, the North–South movement is dominated by solar cycle effects. Investigating the location of the eccentric dipole in spherical coordinates, we note that its northward displacement in latitude has suddenly decreased from 0.069°/yr to 0.014°/yr in 2011, i.e. during the time interval investigated here. The associated particle flux change however remains small when compared to the oscillations of the anomaly during the solar cycle and cannot be detected. In contradiction with Fürst et al. (2009) we conclude that rapid changes of the main field cannot be detected in particle flux measurements.

Our results hold for the 16.5 yr time interval of the analysis. We expect also that our findings will not be altered when data for a complete (Hale) 22 yr cycle and both polarities of the solar magnetic field are available. On secular and millennial time-scales, a prediction of the SAA evolution requires forecasts of the geometry and intensity of the geomagnetic main field and of the L-shell distribution of charged particles. Aubert (2015) has investigated the axial dipole decay and the place where the field is minimum at the Earth's surface for the next 100 yr. In this study the spherical harmonic coefficients that most contribute to the cost function are the low order degree terms, precisely those that model the eccentric dipole. The question now is to infer how the flux of particles above the South Atlantic and South America will change in response to the evolution of the magnetic field. Glassmeier et al. (2004) have shown that less particles can be trapped in a weaker magnetic field. We can also anticipate that interactions between protons trapped in the inner radiation belt and the thermosphere will increase as the SAA grows (Roederer and Zhang (2014)). Our time series are too short to detect a trend in the proton flux. We nonetheless think that the methods used in this work are appropriate to identify such a trend if applied to longer series. It would enable us to forecast the impact of the South Atlantic Anomaly on space weather.

Acknowledgements

We want to thank Vincent Noel for providing the CALIOP-SAA dataset used in this work and the NOAA Space Weather Prediction Center for providing the POES data (ftp://satdat.ngdc.noaa.gov). This work has been carried out with financial support for JD by CNES (Centre National d'Etudes Spatiales) and 'UC – Universidade de Coimbra (DPA-56-16-382)'. CITEUC is funded by FCT – Foundation for Science and Technology (UID/Multi/00611/2013) and COMPETE 2020 – Operational Programme Competitiveness and Internationalization (POCI-01-0145-FEDER-006922). We also thank the reviewers for their assistance in evaluating this paper.

References

Aubert, J., 2015. Geomagnetic forecasts driven by thermal wind dynamics in the Earth's core. Geophys. J. Int. 203, 1738–1751.
Auvergne, M., Bodin, P., Boisnard, L., et al., 2009. The CoRoT satellite in flight: description and performance. Astron. Astrophys. 506, 411–424.
Belli, A., Exertier, P., Samain, E., Courde, C., Vernotte, F., Auriol, A., Jayles, C., 2015. Characterization of an ultra stable quartz oscillator thanks to time transfer by laser link (T2L2, Jason-2). In: Joint Conference of the IEEE International Frequency Control Symposium & the European Frequency and Time Forum. FCS, 2015. IEEE, pp. 808–812.
Bloxham, J., Gubbins, D., Jackson, A., 1989. Geomagnetic secular variation. Philos. Trans. R. Soc. Lond. A 329, 415–502.
Boteler, D.H., Pirjola, R.J., 2014. Comparison of methods for modelling geomagnetically induced currents. Ann. Geophys. 32 (9), 1177–1187.
Capdeville, H., Štěpánek, P., Hecker, L., Lemoine, J.-M., 2016. Update of the corrective model for Jason-1 DORIS data in relation to the South Atlantic Anomaly and a corrective model for SPOT-5. Adv. Space Res., in press.
Casadio, S., Arino, O., 2011. Monitoring the South Atlantic Anomaly using ATSR instrument series. Adv. Space Res. 48, 1056–1066.
Christensen, U.R., Aubert, J., Hulot, G., 2010. Conditions for Earth-like geodynamo models. Earth Planet. Sci. Lett. 296, 487–496.
Evans, D., Garrett, H., Jun, I., Evans, R., Chow, J., 2008. Long-term observations of the trapped high-energy proton population ($L < 4$) by the NOAA Polar Orbiting Environmental Satellites (POES). Adv. Space Res. 41 (8), 1261–1268.
Finlay, C.C., Olsen, N., Kotsiaros, N., Gillet, N., Toffner-Clausen, L., 2016. Recent geomagnetic secular variation from Swarm and ground observatories as estimated in the CHAOS-6 geomagnetic field model. Earth Planets Space 68 (112).
Fraser-Smith, A.C., 1987. Centered and eccentric geomagnetic dipoles and their poles, 1600–1985. Rev. Geophys. 25, 1–16.
Fürst, F., Wilms, J., Rothschild, R., Pottschmidt, K., Smith, D., Lingenfelter, R., 2009. Temporal variations of strength and location of the South Atlantic Anomaly as measured by RXTE. Earth Planet. Sci. Lett. 281, 125–133.
Glassmeier, K., Vogt, J., Stadelmann, A., Buchert, S., 2004. Concerning long-term geomagnetic variations and space climatology. Ann. Geophys. 22, 3669–3677.
Gledhill, J.A., 1976. Aeronomic effects of the South Atlantic Anomaly. Rev. Geophys. Space Phys. 14 (2), 173–187.
Hannachi, A., Jolliffe, I.T., Stephenson, D.B., 2007. Empirical orthogonal functions and related techniques in atmospheric science: a review. Int. J. Climatol. 27, 1119–1152.
Hartmann, G., Pacca, I., 2009. Time evolution of the South Atlantic magnetic anomaly. An. Acad. Bras. Ciênc. 81, 243–255.
Heirtzler, J.R., 2002. The future of the South Atlantic anomaly and implications for radiation damage in space. J. Atmos. Sol.-Terr. Phys. 64, 1701–1708.
Hell, N., 2010. The Evolution of the South Atlantic Anomaly Measured by RHESSI. Master's Thesis. Erlangen Centre for Astroparticle Physics.
Heynderickx, D., 1996. Comparison between methods to compensate for the secular motion of the South Atlantic anomaly. Radiat. Meas. 26 (3), 369–373.
Hunt, W.H., Winker, D.M., Vaughan, M.A., Powell, K.A., Lucker, P.L., Weimer, C., 2009. CALIPSO lidar description and performance assessment. J. Atmos. Ocean. Technol. 26, 1214–1228.
Jackson, A., Jonkers, R.T., Walker, M.R., 2000. Four centuries of geomagnetic secular variation from historical records. Philos. Trans. R. Soc. Lond. A 358, 957–990.
Konradi, A., Badhwar, G.D., Bradby, L.A., 1994. Recent space shuttle observations of the South Atlantic anomaly and radiation belt models. Adv. Space Res. 14, 10911–10921.
Lowes, F.J., 1994. The geomagnetic eccentric dipole: fact and fallacies. Geophys. J. Int. 118, 671–679.
Mandea, M., Korte, M., Mozzoni, D., Kotzé, P., 2007. The magnetic field changing over the southern African continent: a unique behaviour. S. Afr. J. Geol. 110, 193–202.
McIlwain, C.E., 1961. Coordinates for mapping the distribution of magnetically trapped particles. J. Geophys. Res. 66 (11), 3681–3691.
Miyoshi, Y., Morioka, A., Misawa, H., 2000. Long term modulation of low altitude proton radiation belt by the Earth's atmosphere. Geophys. Res. Lett. 27, 2169–2172.
Noel, V., Chepfer, H., Hoareau, C., Reverdy, M., Cesana, G., 2014. Effects of solar activity on noise in CALIOP profiles above the South Atlantic Anomaly. Atmos. Meas. Tech. 7, 1597–1603.
Olsen, N., Lühr, H., Sabaka, T., Mandea, M., Rother, M., Tøffner-Clausen, L., Choi, S., 2006. CHAOS – a model of Earth's magnetic field derived from CHAMP, Ørsted, and SAC-C magnetic satellite data. Geophys. J. Int. 166, 67–75.
Olsen, N., Hulot, G., Lesur, V., et al., 2015. The Swarm initial field model for the 2014 geomagnetic field. Geophys. Res. Lett. 42, 1092–1098.
Olson, P., Amit, H., 2006. Changes in Earth's dipole. Naturwissenschaften 93, 519–542.
Olson, P., Hinnov, L.A., Driscoll, P.E., 2014. Nonrandom geomagnetic reversal times and geodynamo evolution. Earth Planet. Sci. Lett. 388, 9–17.
Pais, M.A., Morozova, A.L., Schaeffer, N., 2015. Variability modes in core flows inverted from geomagnetic field models. Geophys. J. Int. 200, 402–420.
Preisendorfer, R.W., 1988. Principal Component Analyses in Meteorology and Oceanography. Elsevier.
Pulkkinen, A., Bernabeu, E., Eichner, J., Beggan, C., Thomson, A.W.P., 2012. Generation of 100-year geomagnetically induced current scenarios. Space Weather 10, S04003.
Qin, M., Zhang, X., Ni, B., Song, H., Zou, H., Sun, Y., 2014. Solar cycle variations of trapped proton flux in the inner radiation belt. J. Geophys. Res. Space Phys. 119 (12), 9658–9669.
Roederer, J.G., Zhang, H., 2014. Dynamics of Magnetically Trapped Particles, 2nd edn. Springer.
Schaefer, R., Paxton, L., Selby, C., Ogorzalek, B., Romeo, G., Wolven, B., Hsieh, S.-Y., 2016. Observation and modeling of the South Atlantic Anomaly in low Earth orbit using photometric instrument data. Space Weather 14, 330–342.

Selesnick, R.S., Baker, D.N., Jaynes, A., Li, X., Kanekal, S.G., Hudson, M.K., Kress, B.T., 2014. Observations of the inner radiation belt: CRAND and trapped solar protons. J. Geophys. Res. Space Phys. 119, 6541–6552.

Solomon, S.C., Qian, L., Burns, A.G., 2013. The anomalous ionosphere between solar cycles 23 and 24. J. Geophys. Res. Space Phys. 118 (10), 6524–6535, 2013JA019206.

Vacaresse, A., Boscher, D., Bourdarie, S., Blanc, M., Sauvaud, J.A., 1999. Modeling the high-energy proton belt. J. Geophys. Res. 104 (A12), 28601–28613.

Vernov, S.N., Gorchakov, E.V., Shavrin, P.I., Sharvina, K.N., 1967. Radiation belts in the region of the South-Atlantic magnetic anomaly. Space Sci. Rev. 7, 490–533.

Von Storch, H., Navarra, A., 1995. Analyses of Climate Variability-Applications of Statistical Techniques. Springer.

Zou, H., Li, C., Zong, Q., Parks, G.P., Pu, Z., Chen, H., Xie, L., Zhang, X., 2015. Short-term variations of the inner radiation belt in the South Atlantic anomaly. J. Geophys. Res. Space Phys. 120, 4475–4486.